Metals and Materials International (2018) 24:1412–1421
https://doi.org/10.1007/s12540-018-0127-2

Effects of Grain Size on the Fatigue Properties in Cold-Expanded Austenitic HNSs

Jong-Ho Shin[1] · Young-Deak Kim[1] · Jong-Wook Lee[1]

Received: 7 February 2018 / Accepted: 15 April 2018 / Published online: 9 May 2018

Abstract
Cold-expanded austenitic high nitrogen steel (HNS) was subjected to investigate the effects of grain size on the stress-controlled high cycle fatigue (HCF) as well as the strain-controlled low cycle fatigue (LCF) properties. The austenitic HNSs with two different grain sizes (160 and 292 μm) were fabricated by the different hot forging strain. The fine-grained (FG) specimen exhibited longer LCF life and higher HCF limit than those of the coarse-grained (CG) specimen. Fatigue crack growth testing showed that crack propagation rate in the FG specimen was the same as that in the CG specimen, implying that crack propagation rate did not affect the discrepancy of LCF life and HCF limit between two cold-expanded HNSs. Therefore, it was estimated that superior LCF and HCF properties in the FG specimen resulted from the retardation of the fatigue crack initiation as compared with the CG specimen. Transmission electron microscopy showed that the effective grain size including twin boundaries are much finer in the FG specimen than that in the CG specimen, which can give favorable contributions to strengthening.

Keywords Cold working · Forging · Fatigue · Fracture · Twinning

1 Introduction

High nitrogen steel (HNS) has received a great deal of attention owing to the excellent properties such as good strength-ductility balance and resistance to localized corrosion. Extensive literatures on deformation behavior of austenitic HNS are available, and they are concerned with solid-solution hardening together with cold-work strengthening and increased tendency to form planar dislocation structure associated with stacking fault energy (SFE) [1–8]. Owing to progresses in manufacturing technologies, some commercial grades of austenitic HNS are now available for applications in power generation and oil-field industries as well as biomaterials [9, 10]. As a part of ongoing efforts to wider application of austenitic HNS, many attempts have been made to improve their mechanical properties and reliability for structural applications.

One of the most successful applications in austenitic HNS is the retaining ring used for fixing a copper coil on the generator rotor rotating with high speed in the power plant. In order to avoid the unpredictable failure of a component induced by fatigue crack propagation, fatigue properties play important roles in the operating condition and safety requirements for the power plant and generator components. From engineering point of view, both low cycle fatigue (LCF) and high cycle fatigue (HCF) properties are the critical mechanical properties: LCF are related to the deformation strain conditions in the course of a repeated start/stop period; HCF properties are associated with the vibrational loading conditions during generator operating.

It is well known that grain size refinement is an effective method to improve tensile strength and fatigue properties in austenitic stainless steel [11–15]. However, it has been shown in recent investigation that grain size in austenitic HNS does not influence on fatigue crack initiation [16] and a preferential site for fatigue crack initiation is not grain boundaries but annealing twin boundaries [17]. Only limited

✉ Jong-Wook Lee
jwook.lee@doosan.com

Jong-Ho Shin
jongho.shin@doosan.com

Young-Deak Kim
youngdeak.kim@doosan.com

[1] Materials and Manufacturing Technology Development Center, Corporate Research and Development Institute, Doosan Heavy Industries and Construction Co., LTD., Changwon 51711, Republic of Korea

data on the fatigue properties of cold-expanded austenitic HNS, which is an essential prerequisite for engineering application, are available in the literature.

Therefore, the purpose of this paper is to understand the effects of grain size on the fatigue properties of cold-expanded austenitic HNSs for retaining ring exposing to high stress and cyclic loading conditions. This paper is intended to figure out the dominant step in fatigue fracture steps influencing these fatigue properties.

2 Experimental Procedure

Chemical composition of austenitic HNS examined in this study was listed in Table 1. The 30 ton ingot was melted using Argon Oxygen Decarburization (AOD) method and then, remelted using Electro-Slag Remelting (ESR) process to improve the cleanliness. The ESR ingot was forged to ring shape of ID 630 mm × OD 810 mm × H 850 mm at the temperature range of 900–1250 °C. In order to control grain size, different strains of 10 and 25% were applied at the forging temperature range, and they were solution heat treated at 1050 °C for 5 h followed by water quenching. The grain size was measured using a mean linear intercept method (ASTM E112). The two rings were cold-expanded to the size of ID 900 mm × OD 1000 mm × H 770 mm at room temperature. After cold expansion, stress relieving treatment was carried out at 400 °C for 5 h and then, air-cooled.

The microstructures of as-cold-expanded austenitic HNSs were observed for the middle part of the retaining ring thickness. They were characterized by optical microscope (OM, ZEISS Axioplan) and scanning transmission electron microscope (STEM, JEOL JEM-2100F). The specimens were mechanically polished and then, chemically etched with a Glyceregia reagent (30 ml hydrochloric acid, 20 ml glycerin, and 10 ml nitric acid).

All the specimens for tensile and fatigue testing were prepared at the middle wall of retaining ring. The direction of the specimens was parallel to expansion axial direction. Tensile test was carried out at room temperature using an Instron 5585. For LCF test, the cylindrical specimens of 7 mm diameter and 12.5 mm gage length were prepared. LCF test was carried out under fully reversed axial strain control mode using a triangular waveform at room temperature (ASTM E606). The strain rate was 0.01 s^{-1} and the total strain amplitude ($\Delta\varepsilon_t/2$) was changed from 0.005 to 0.016 (Instron 8801). Fatigue life was defined as a 30% load drop point of a stabilized peak load. After LCF test, crack propagation was observed with scanning electron microscope (SEM, HITACH S-3400N).

The cylindrical specimen of 5 mm diameter for high cycle fatigue (HCF) was prepared at the middle wall of retaining ring. The direction of the specimen was parallel to expansion axial direction. The specimens were mechanically grinded and polished to a mirror-like-finish. HCF test was carried out under a load control at a stress ratio of $R = -1$ ($R = \sigma_{min}/\sigma_{max}$) and the frequency of 10 Hz using a sinusoidal waveform at room temperature (ASTM E466).

Compact tension specimens with a thickness of 12.5 mm and width of 50 mm was prepared for fatigue crack propagation. Fatigue pre-cracking process was carried out at the load ratio, $R = 0.1$ and the crack length of 3 mm. Fatigue crack propagation test was carried out at a constant stress ratio of $R = 0.1$ under a constant frequency of 10 Hz at room temperature (ASTM E647). The crack length was measured continuously by the compliance method with a crack mouth clip gauge. Fatigue crack propagation rate was calculated with decreasing stress intensity factor range from 25 up to the near-threshold region and with increasing stress intensity factor range from 25 up to the near-accelerated crack propagation region.

3 Results

3.1 Microstructures and Tensile Properties

The austenitic HNS with coarse grain (CG) was hot-forged by 10% strain, whereas that with fine grain (FG) was hot-forged by 25% strain. The average grain size of the CG and FG specimens was measured to be 292 and 160 μm, respectively. The microstructure was confirmed to be austenite single phase composed of annealing twins and slip bands as shown in Fig. 1. Annealing twins and slip bands were formed during solution treatment and cold-expansion, respectively. Slip bands were observed within all of grains and any precipitate was not observed on grain and annealing twin boundaries. High manganese and nitrogen concentration stabilized austenitic structure against martensitic transformation after cold-expansion [18]. The M_{d30} (50% α′-martensite presents after 30% tensile deformation) temperatures calculated from empirical equations reported in the literature are listed in Table 2 [19]. The calculated M_{d30} temperatures are quite low, implying higher stability of austenitic structure at room temperature.

Table 1 Chemical composition of high nitrogen austenitic stainless steel

Composition	C	Si	Mn	Cr	V	N
wt%	0.04–0.06	0.25–0.5	17.5–19.5	17.5–19.0	0.03–0.08	0.60

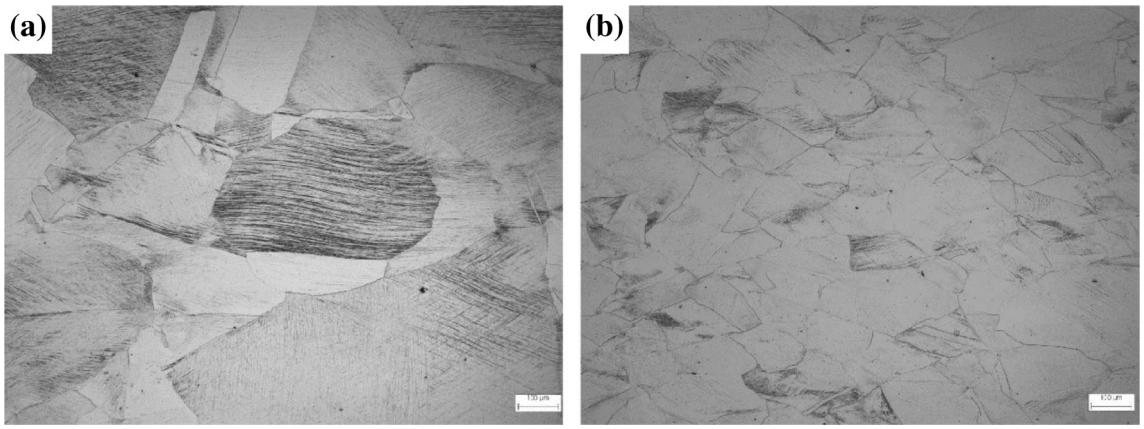

Fig. 1 Optical microstructure after cold-expansion of **a** the CG specimen and **b** the FG specimen

Table 2 M_{d30} temperature calculated by various equations

Angel[a] M_{d30} (°C)	Gladman[b]	Nohara[c]	Sjöberg[d]
− 316.9	− 233.8	− 222.1	− 592.3

[a]413–462[%C + %N] − 9.2[%Si] − 8.1[%Mn] − 13.7[%Cr] − 9.5[%Ni] − 18.5[%Mo]

[b]497–462[%C + %N] − 9.2[%Si] − 8.1[%Mn] − 13.7[%Cr] − 20[%Ni] − 18.5[%Mo]

[c]551–462[%C + %N] − 9.2[%Si] − 8.1[%Mn] − 13.7[%Cr] − 29[%Ni + %Cu] − 18.5[%Mo] − 68[%N]

[d]608–515[%C]–821[%N] − 7.8[%Si] − 12[%Mn] − 13[%Cr] − 34 [%Ni] − 6.5[Mo]

TEM micrographs showing typical deformation microstructures of the CG and FG specimens after cold-expansion were shown in Fig. 2. Sharp parallel traces along close-packed {111} planes of austenite matrix were distinguished, and they were intersected with each other. A closer examination of selected area diffraction (SAD) patterns revealed that they were identified as deformation twinning induced by cold-expansion and have $\{111\}\langle 11\bar{2}\rangle$ crystallographic component [20]. In both CG and FG specimens, primary and conjugate twinning systems were operated, and the angles between primary and conjugate system was found to be 70.53, corresponding to the simple homogenous shear of $a/\sqrt{2}$ in $(1\bar{1}0)$ plane. Comparing with the CG specimen, deformation twinning in the FG specimen had much finer size and distributed uniformly. It is known that the deformation twin formed after plastic deformation can act as an effective barrier against subsequent motion of dislocations. Thus, it is conceivable that the effective grain size including twin boundaries are much finer in the FG specimen than that in the CG specimen, which can give favorable contributions to strengthening owing to increase in pinning force for migrating dislocations [21, 22].

Figure 3 showed the stress–strain curve obtained from the CG and FG specimens at room temperature. The CG specimen had 928 MPa in yield strength (YS) and 1098 MPa in ultimate tensile strength (UTS), whereas the FG specimen showed 980 MPa in YS and 1140 MPa in UTS, respectively. The FG specimen exhibited higher YS and UTS than the CG specimen. This results were associated with fine grain size and fine effective grain size including twin boundaries. Strain hardening during tensile test was rarely detected in the both specimens due to the effect of pre-cold working during cold-expansion process. The FG specimen showed the gradual decrease in strength with increasing strain after UTS, whereas the CG specimen showed suddenly dropped strength over 0.257 in strain.

3.2 LCF Properties

Figure 4 showed cyclic peak stress responses under the total strain amplitude range ($\varepsilon_t/2$) of 0.005–0.012. It was found that the CG and FG specimens showed similar cyclic peak stress responses. At all of total strain amplitude, the peak stress was decreased rapidly in the initial stage of cycle and then, it showed a long saturation stage until final failure. Where the saturation stage is determined as a stage such that the slope of the peak stress with respect to number of cycle is constant. Cyclic softening behavior observed in the both CG and FG specimens through a whole fatigue life was attributed to the pre-strain during cold-expansion [23, 24]. At all of total strain amplitude, macro-crack of the CG specimens initiated lower cycle number than that of FG specimens. Where macro-crack initiated corresponds to the cycle number showing a rapid decrease of peak stress from saturation stage [25].

In order to quantify the degree of cyclic softening, softening ratio (R_{sr}) is defined as [26]:

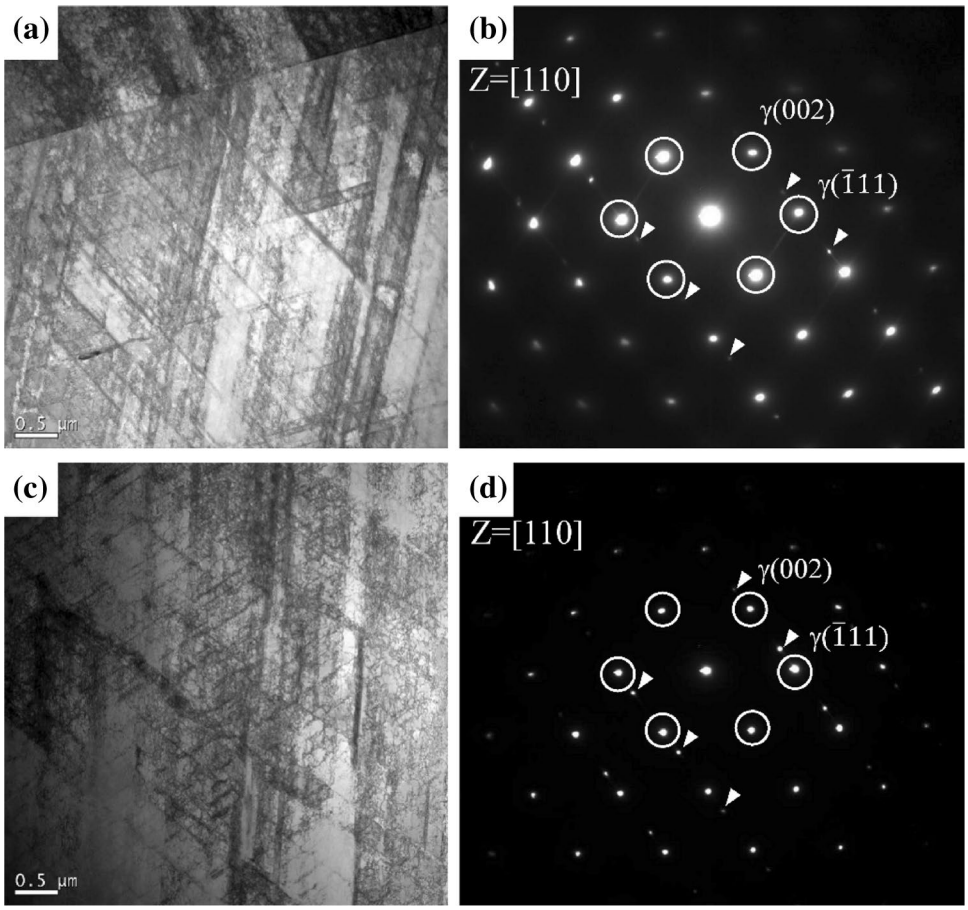

Fig. 2 TEM micrographs of mechanical twin: **a** TEM bright field images and **b** SAD pattern in the CG specimen. **c** TEM bright field image and **d** SAD pattern in the FG specimen. Circle represents matrix reflection and arrow represents twined reflection

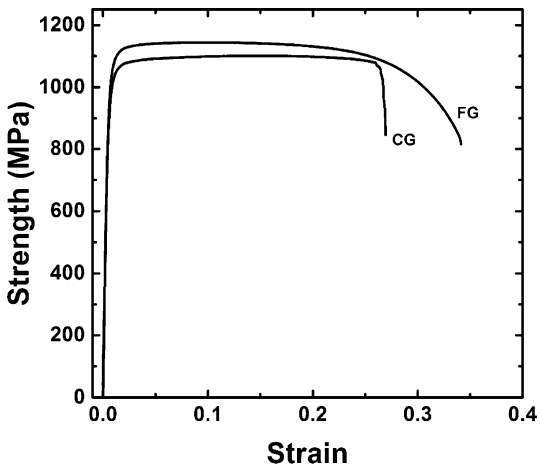

Fig. 3 Variation of strength-strain curve in the CG and FG specimens after cold-expansion

$$R_{sr} = \frac{\sigma_{max} - \sigma_{max}|N_s/2}{\sigma_{max}} \quad (1)$$

where σ_{max} is the maximum peak stress in fatigue life and $\sigma_{max}|N_s/2$ is the peak stress at the middle of the saturation stage. The degree of cyclic softening changed with total strain amplitude at different grain size as shown in Fig. 5. At the FG specimen, cyclic softening increased with the increase of total strain amplitude up to 0.01 and then, it was saturated. On the other hand, cyclic softening at the CG specimen increased up to total strain amplitude of 0.009 and then, it was continue to decrease with increase of total strain amplitude. Cyclic softening behavior has been reported in the materials which are cold-worked or have high initial dislocation density [27, 28].

The total strain amplitude ($\Delta\varepsilon_t/2$), elastic strain amplitude ($\Delta\varepsilon_e/2$), and plastic strain amplitude ($\Delta\varepsilon_p/2$) with the number of reversals to failure ($2N_f$) was shown in Fig. 6. Elastic strain and plastic strain amplitudes were obtained from the elastic strain and plastic strain components at the total strain amplitude from the hysteresis loop at half of the number of cycles to failure. The relationship between total strain amplitude and fatigue life is expressed by Coffin–Manson equation [29]:

$$\frac{\Delta\varepsilon_t}{2} = \frac{\Delta\varepsilon_e}{2} + \frac{\Delta\varepsilon_p}{2} = \frac{\sigma_f'}{E}(2N_f)^b + \varepsilon_f'(2N_f)^c \quad (2)$$

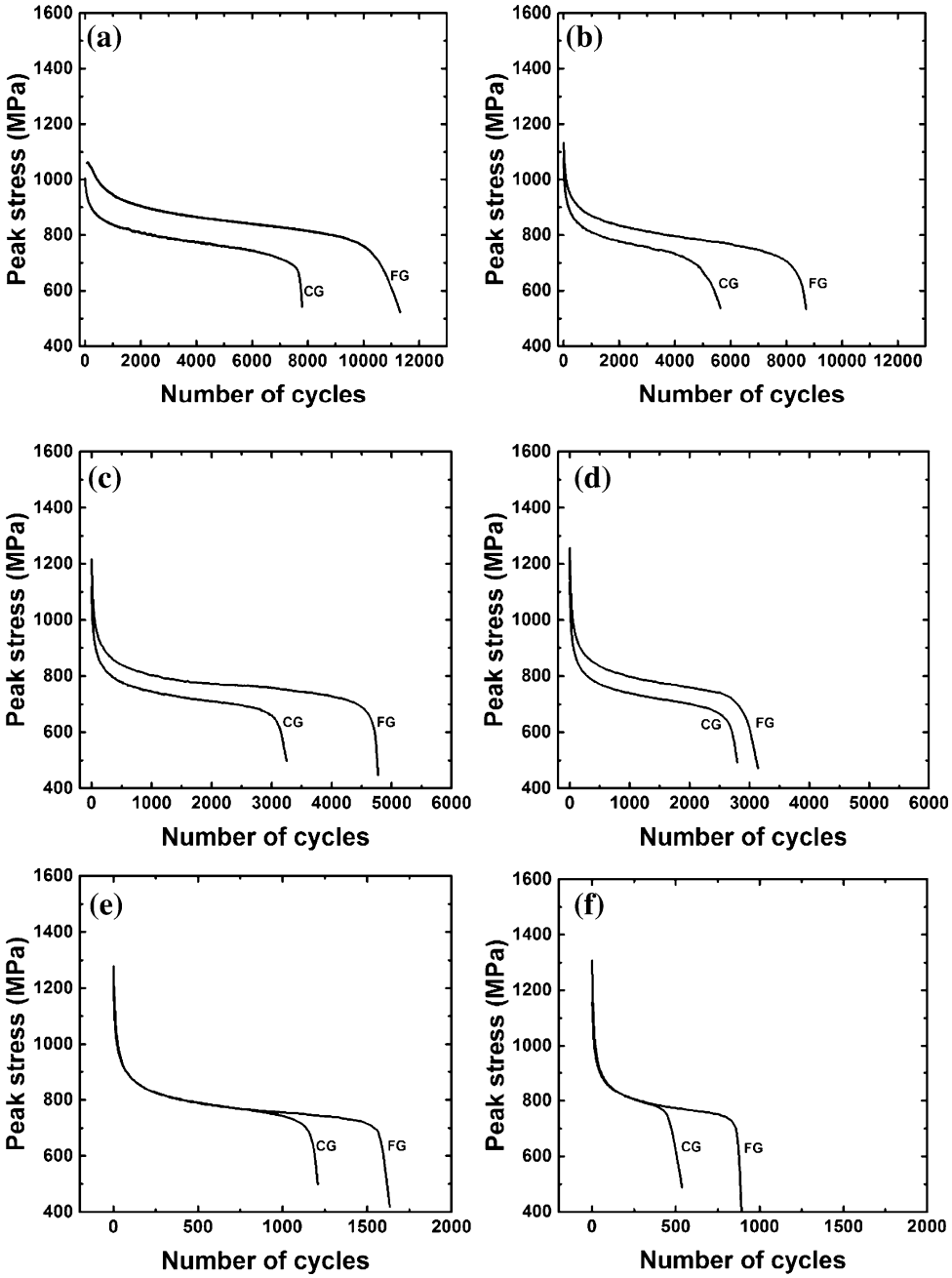

Fig. 4 Cyclic stress responses of the CG and FG specimens at room temperature; **a** $\Delta\varepsilon_t/2=0.005$, **b** $\Delta\varepsilon_t/2=0.006$, **c** $\Delta\varepsilon_t/2=0.007$, **d** $\Delta\varepsilon_t/2=0.008$, **e** $\Delta\varepsilon_t/2=0.01$, **f** $\Delta\varepsilon_t/2=0.012$

where $\Delta\varepsilon_t/2$, $\Delta\varepsilon_e/2$, and $\Delta\varepsilon_p/2$ are total strain amplitude, elastic strain amplitude, and plastic strain amplitude, respectively. $2N_f$, σ'_f, E, and ε'_f are the number of reversals to failure, fatigue strength coefficient, young's modulus, and fatigue ductility coefficient, respectively. Elastic strain amplitude and plastic strain amplitude with respect to fatigue life ($2N_f$) were linear in both of the CG and FG specimens as shown in Fig. 6a, b. The LCF parameters obtained from the different grain size specimens of the cold-expanded austenitic HNS was listed in Table 3. As compared with elastic strain parameters in the CG specimen, those in the FG specimen showed a slightly lower σ'_f/E and absolute value of b. The FG specimen also showed a higher ε'_f and a slightly higher absolute value of c, indicating a larger slop in the fatigue life curve. Total strain amplitude with the number of reversals to failure ($2N_f$) was shown in Fig. 6c. It was clearly found that fatigue life in the FG specimen was longer than that of the CG specimen at the low and high strain amplitude. The results imply that grain size refinement can effectively improve the LCF life in the cold-expanded austenitic HNS.

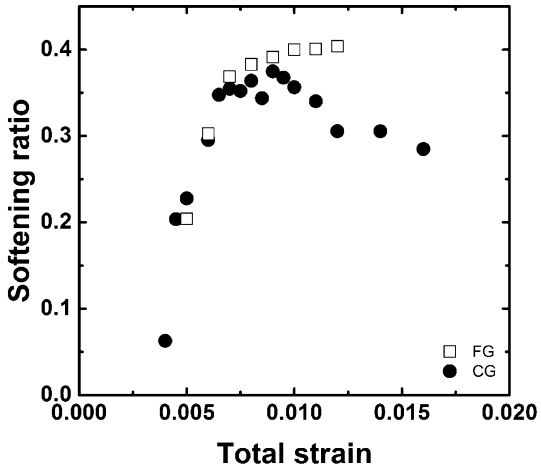

Fig. 5 Variation of softening ratio with total strain

3.3 HCF Properties

Figure 7 showed the HCF behaviors in the cold-expanded austenitic HNSs, in which the solid symbols indicated that the specimen was not fractured during HCF test. Fatigue strength at 10^7 cycles was defined as the fatigue limit. Although a definite fatigue limit was the characteristics of HCF behavior in ferrous alloys, this behavior even in the cold-worked austenitic HNS was also observed. The FG specimen showed higher fatigue limit than the CG specimen by about 72 MPa. The fatigue life was increased with decreasing cyclic stress as shown in S–N curve. The S–N curve was described using the Basquin equation [29, 30]:

$$\sigma_a = \sigma_f' (2N_f)^b \tag{3}$$

where σ_a, σ_f', and b are the normal stress amplitude, the fatigue strength coefficient, and the Basquin exponent, respectively. The fitted fatigue strength coefficient and the Basquin exponent were listed in the Table 4. The Basquin equation was just applied for the number of cycle less than 10^7. The FG specimen showed a higher value of the fatigue strength coefficient, indicating a higher stress amplitude in the S–N curves.

3.4 Fatigue Crack Propagation

Fatigue crack propagation rate was calculated with changing stress intensity factor range at the steady-state crack propagation region. Figure 8 showed a linear increase in fatigue crack propagation rate with the increase in stress intensity factor range in both FG and CG specimens. The

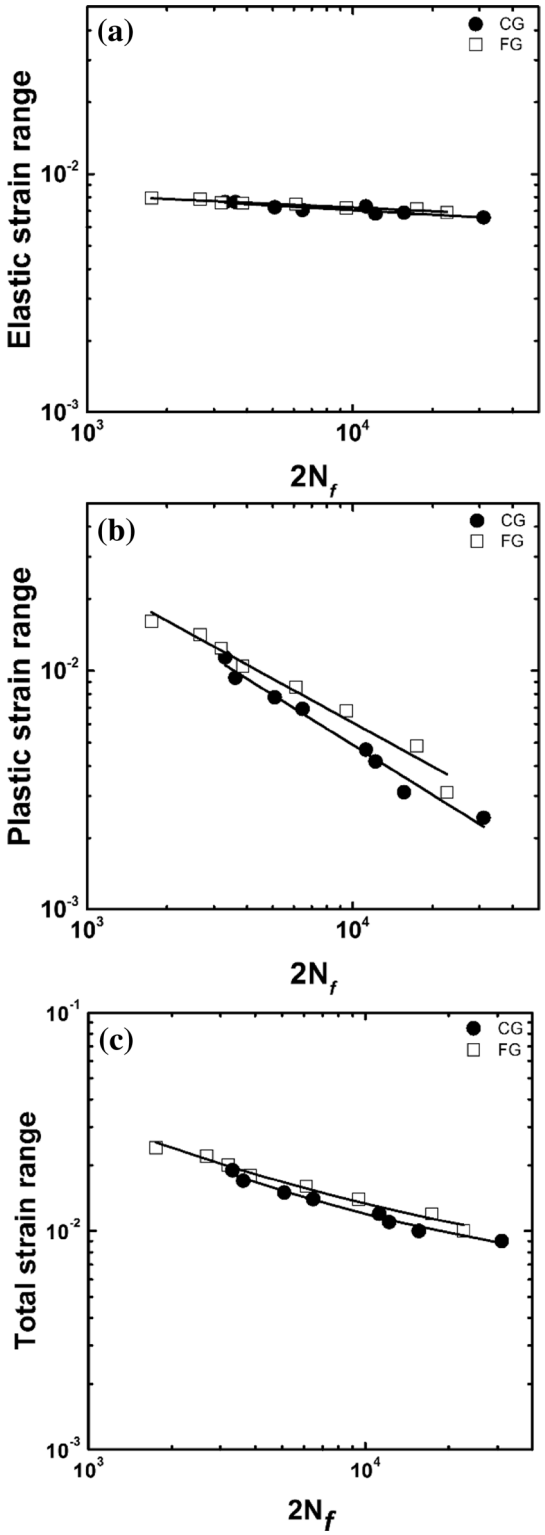

Fig. 6 LCF lifetime curve versus the number of reversals to failure in the CG and FG specimens: **a** elastic strain amplitude, **b** plastic strain amplitude and **c** total strain amplitude

Table 3 LCF parameters for coarse and fine grain specimens

Parameters	σ_f'/E	b	ε_f'	c
CG	0.0069	−0.073	0.4211	−0.558
FG	0.0059	−0.05	0.8260	−0.608

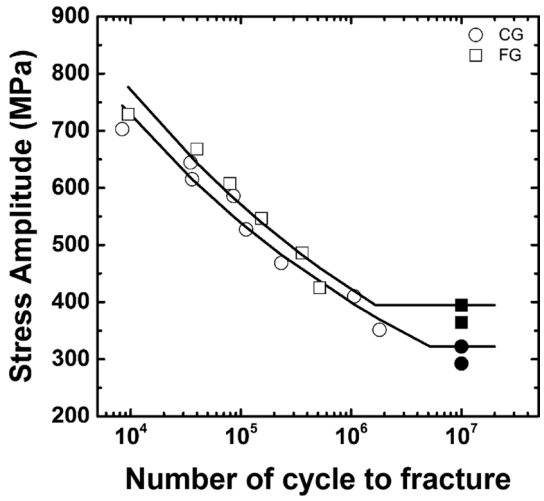

Fig. 7 S–N curves in the CG and FG specimens

Table 4 HCF parameters for coarse and fine grain specimens

Parameters	σ_f'	b
CG	2639.73	−0.130
FG	2822.28	−0.131

fatigue crack propagation rate was described using Paris equation [31]:

$$\frac{d_a}{d_N} = C(K)^m \tag{4}$$

where C, ΔK, and m are constant, stress intensity factor range, and constant, respectively. The fitted constants in the FG and CG specimens were listed in Table 5. C and exponent m values were nearly similar to each other in the FC and CG specimens. It is well known that these constants are influenced by material microstructure, environment, temperature, and load ratio ($R = \sigma_{min}/\sigma_{max}$) [32]. These results imply that crack propagation rate in the FG and CG specimens was similar under low cycle fatigue and high cycle fatigue conditions. Therefore, fine grain size does not play any role to prevent fatigue crack propagation under the experimental conditions in the cold-expanded austenitic HNS.

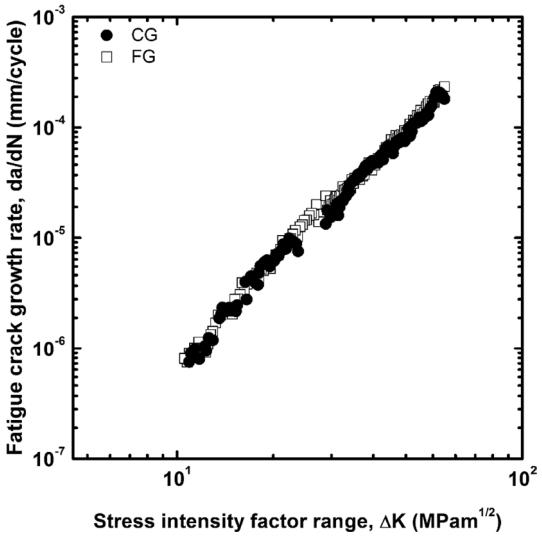

Fig. 8 Variation of fatigue crack growth rate with stress intensity factor range in the CG and FG specimens

Table 5 Fatigue crack propagation parameters for coarse and fine grain specimens

Parameters	C	m
CG	4.96×10^{-10}	3.19
FG	4.87×10^{-10}	3.17

3.5 Crack Propagation Path and Fractography

Figure 9 showed crack propagation path during LCF. Three different locations of crack initiation were observed in the CG specimen so that crack propagation length in the CG specimen was relatively shorter than that in the FG specimen. In some cases, crack propagation along slip band, grain boundaries and annealing twin boundaries was observed locally, but crack mainly propagated through transgranular in a perpendicular direction to the applied stress.

After HCF test, fractograph represented three different regions of the fatigue fracture surface including the crack initiation, the crack propagation and the final fracture regions, denoted as A, B and C as shown in Fig. 10. Mark "A" in Fig. 10a, c indicates HCF crack initiates on the surface of the CG and FG specimens, and the CG specimen showed multiple crack initiation on the surface. Any inclusion at the crack initiation region was not observed due to the high purity guaranteed by ESR process. Crack propagated inward in the transgranular mode with the striation formation as shown in Fig. 10b, d, and perpendicular direction to the applied cyclic loading.

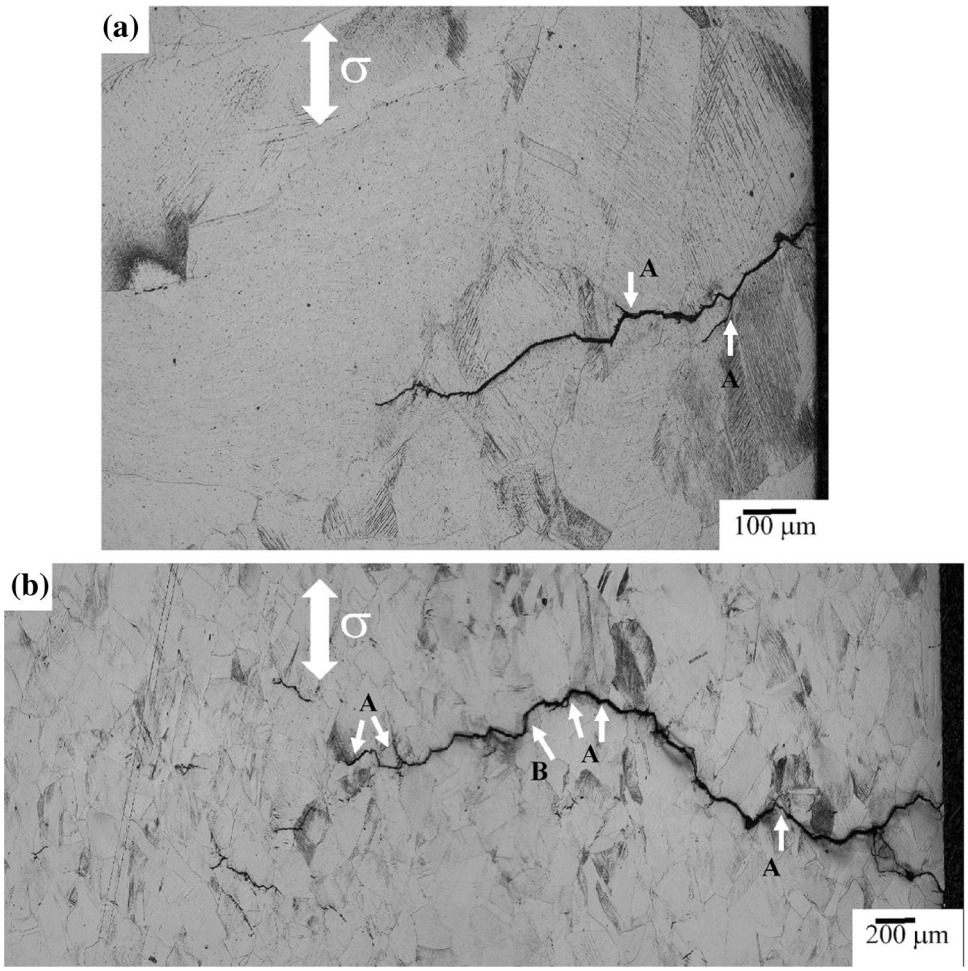

Fig. 9 Optical micrographs of LCF cracks at $\Delta\varepsilon_t/2 = 0.005$ in **a** the CG specimen and **b** the FG specimen. Crack mainly propagated through slip band, mark "A" indicates crack propagation through grain boundary and mark "B" indicates crack propagation through twin boundary

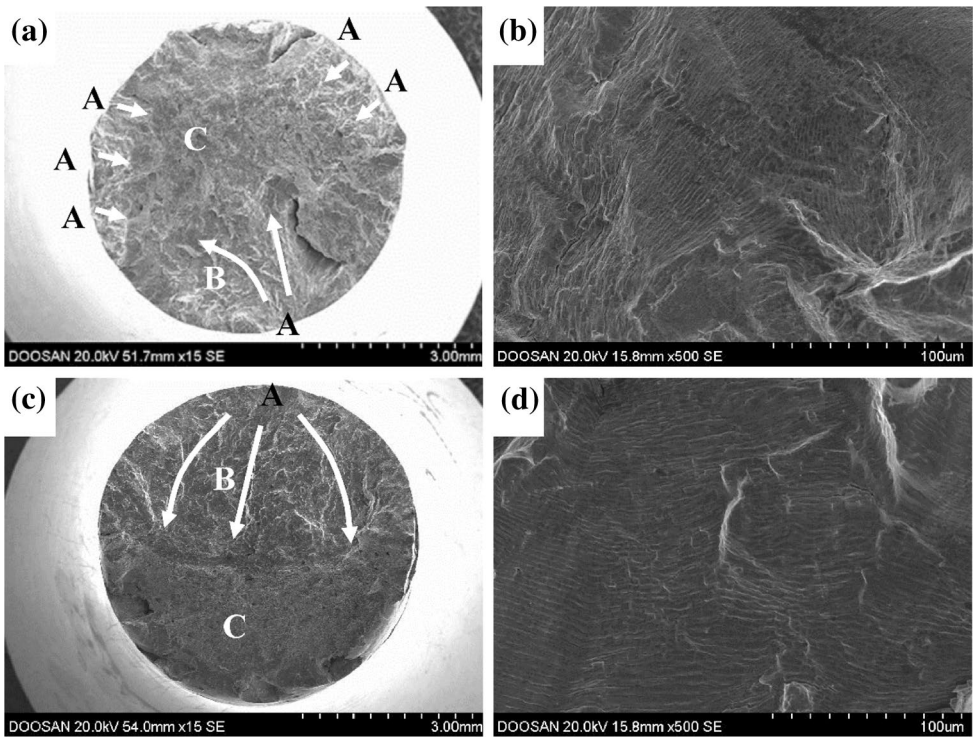

Fig. 10 HCF fracture surface of **a** the CG specimen at $\sigma = 644$ MPa, **b** higher magnification view of mark "B" region in the CG specimen, **c** the FG specimen at $\sigma = 668$ MPa and **d** higher magnification view of mark "B" region in the FG specimen

4 Discussions

4.1 Tensile Behavior

The strength-strain curve shown in Fig. 3 represented that strength ratio (0.2% YS/UTS) was 0.845 in the CG specimen and 0.859 in the FG specimen. This high strength ratio resulting from cold-expansion is associated with high dislocation density and the intersection between mechanical twins as shown in previous study [20]. Dislocations were generated or rearranged during cold-expansion process and then, they mutually acted as a barrier to their movement. During tensile deformation, deformation twin formed during cold-expansion process also acted as a barrier to dislocation movement as the effective grain boundaries [21, 22]. Therefore, high dislocation density and deformation twin boundaries formed during cold-expansion process resulted in increasing yield strength and reducing elongation.

The reason why the FG specimen has higher YS than the CG specimen is that the FG specimen has regularly small grain size and small effective grain size consisting of twin boundaries, reducing the mean free path of dislocation. The FG specimen showed a smooth decrease of strength in strain-to-failure in S–S curve shown in Fig. 3. This tensile behavior can occur in uniform deformation along cross-section of the tensile specimen, resulting from the uniformly small grain size. The drop of strength near strain-to-failure can occur in the tensile specimen with the irregular and coarse grain size shown in Fig. 1. When grain size is coarse, a stress concentration at a location intersecting between slip band and grain boundaries or annealing twin boundaries is large due to long slip band as compared with small grain size [33]. Therefore, micro-crack can be formed easily on the boundaries of coarse grain compared to the case of fine grain. The connection of micro-crack on the coarse grain boundaries at a strain during tensile deformation can result in the drop of strength.

4.2 LCF and HCF Behavior

It is well known that fatigue properties depend on microstructure, grain size and degree of pre-strain [34]. The effects of grain size on fatigue behavior in cold-expanded austenitic HNSs were investigated in this paper. The specimens of two different grain size had the same degree of cold-expansion and the same structure. However, the results of LCF and HCF tests showed that the FG specimen had longer LCF life and higher HCF limit than the CG specimen as shown in Figs. 6 and 7, respectively. These fatigue properties can be controlled by the resistance to crack initiation and crack propagation rate. For the cold-expanded austenitic HNSs, the CG and FG specimens showed very similar crack propagation rate as shown in Fig. 8, which meant that crack propagation rate did not influence on the discrepancy of LCF life and HCF limit in the CG and FG specimens. These results were in accordance with crack propagation mode in cold-expanded austenitic HNS since crack propagation did not occur in any specific microstructural features such as slip band, grain and annealing twin boundaries as shown in Figs. 9 and 10 but took place along transgranular direction perpendicular to cyclic loading.

The other factor influencing on fatigue properties is the resistibility to fatigue crack initiation. Fatigue properties could be improved when fatigue crack initiation was retarded. During fatigue test, dislocation movement is restricted on the slip bands so that the slip band can result in the stress concentration when it encounters with grain and annealing twin boundaries. The stress concentration can be larger in the specimen with the coarse grain as compared with the FG specimen since the coarse grain has longer slip band [33]. Therefore, the initiation of fatigue crack was easer in the specimen with the coarse grain so that the FG specimen showed longer LCF life and higher HCF limit than the CG specimen. Because the FG and CG specimens showed nearly similar fatigue crack propagation rate, it was considered that the retardation of fatigue crack initiation dominated the strain-controlled LCF life and the stress-controlled HCF limit in the cold-expanded austenitic HNSs. For the stress-controlled HCF test, the FG specimen with higher YS had lower strain to reach the same stress as compared to the CG specimen with lower YS so that stress concentration on grain boundaries could be lower in the FG specimen.

5 Conclusions

1. Cold-expanded austenitic HNS exhibited high YS and UTS, which were attributed to high dislocation density and mechanical twin working as a barrier of dislocation movement.
2. The effective grain size including twin boundaries was much finer in the FG specimen than that in the CG specimen, which can contribute to improve strength.
3. Cold-expanded austenitic HNS exhibited cyclic softening behavior during LCF test, of which the degree was influenced by total strain amplitude and grain size.
4. The grain size refinement enhanced the LCF life and the HCF limit in the cold-expanded austenitic HNS. The improvement in the LCF life and the HCF limit in the FG specimen as compared with those in the CG specimen was due to the retardation of fatigue crack initiation, not due to slow fatigue crack propagation rate.

Acknowledgements This research was supported financially by Doosan Heavy Industries & Construction R&D fund and the Materials &Components Technology Development Program (10038377) funded by the Ministry of Trade, Industry and energy (MOTIE) of Republic of Korea.

References

1. Y. Kim, Y. Park, J. Corr. Sci. Kor. **18**, 67 (1989)
2. H. Ha, H. Kwon, Electro. Acta **52**, 2175 (2007)
3. M.L.G. Byrnes, M. Grujicic, W.S. Owen, Acta Metall. **35**, 1853 (1987)
4. E. Werner, Mater. Sci. Eng., A **101**, 93 (1988)
5. J.W. Simmons, Mater. Sci. Eng., A **207**, 159 (1996)
6. G. Saller, K. Spiradek-Hahn, C. Scheu, H. Clemens, Mater. Sci. Eng., A **427**, 246 (2006)
7. P. Mullner, C. Solenthaler, P. Uggowitzer, M.O. Speidel, Mater. Sci. Eng., A **164**, 164 (1993)
8. D.T. Liewellyn, Mater. Sci. Technol. **13**, 389 (1997)
9. K. Orita, Y. Ikeda, T. Iwadate, J. Ishizaka, ISIJ Int. **30**, 587 (1990)
10. J.W. Simmons, Acta Mater. **45**, 2467 (1997)
11. A.D. Schino, J.M. Kenny, Mater. Lett. **57**, 3182 (2003)
12. A. Chlupova, J. Man, I. Kubena, J. Polak, L.P. Karkalainen, Proc. Eng. **74**, 147 (2014)
13. S. Kang, J. Jung, M. Kang, W. Woo, Y. Lee, Mater. Sci. Eng., A **652**, 212 (2016)
14. O. Bouaziz, S. Allain, C. Scott, Scr. Mater. **58**, 484 (2008)
15. A. Järvenpää, L.P. Karjalainen, M. Jaskari, Int. J. Fatigue **65**, 93 (2014)
16. A. Di Schino, M. Barteri, J.M. Kenny, J. Mater. Sci. Lett. **22**, 1511 (2003)
17. M. Roach, S. Wright, J. Lemons, L. Zardiackas, Mater. Sci. Eng., A **586**, 382 (2013)
18. T. Lee, C. Oh, S. Kim, Scr. Mater. **58**, 110 (2008)
19. A. Frehn, E. Ratte, W. Bleck, in *Proceedings 7th International Conference High Nitrogen Steels*, eds by N. Akdut, B.C. Decooman, J. Foct (GRIPS Media GmbH, Ostend, Belgium, 2004), p. 447
20. J. Shin, J. Lee, Mater. Charact. **91**, 19 (2014)
21. P. Changizian, A. Zarei-Hanzaki, H. Abedi, Mater. Sci. Eng., A **558**, 44 (2012)
22. H.E. Kadiri, J. Kapil, A.L. Oppedal Jr., L.G. Hector, S.R. Agnew, M. Cherkaoui, S.C. Vogel, Acta Mater. **61**, 3549 (2013)
23. S. Hong, S. Yoon, S. Lee, Int. J. Fatigue **25**, 1293 (2003)
24. S. Hong, S. Lee, T. Byun, Mater. Sci. Eng., A **457**, 139 (2007)
25. Y. Luo, C. Huang, R. Tian, Q. Wang, J. Iron Steel Inst. **20**, 50 (2007)
26. Q. Zhou, L. Qian, J. Meng, L. Zhao, F. Zhang, Mater. Des. **85**, 487 (2015)
27. P. Guo, L. Qian, J. Meng, F. Zhang, L. Li, Mater. Sci. Eng., A **584**, 133 (2013)
28. S. Hong, S. Lee, Int. J. Fatigue **26**, 899 (2004)
29. G.E. Dieter, *Mechanical Metallurgy* (McGraw-Hill, London, 1988)
30. M. Mokhtarishirazabad, S.M.A. Boutorabi, M. Azadi, M. Nikravan, Mater. Sci. Eng., A **587**, 179 (2013)
31. P. Paris, F. Erdogan, J. Fluids Eng. **85**, 528 (1963)
32. Y. Uematsu, M. Akita, M. Nakajima, K. Tokaji, Int. J. Fatigue **30**, 642 (2008)
33. S. Kang, J. Jung, M. Kang, W. Woo, Y. Lee, Mater. Sci. Eng., A **652**, 212 (2016)
34. A.S. Hamada, L.P. Karjalainen, J. Puustinen, Mater. Sci. Eng., A **517**, 68 (2009)